



# On the fatigue behavior of a tool steel manufactured by powder bed based additive manufacturing—a comparison between electron- and laserbeam processed AISI H13

M. Kahlert<sup>1</sup> · M. Vollmer<sup>1</sup> · T. Wegener<sup>1</sup> · T. Niendorf<sup>1</sup>

Received: 15 May 2023 / Accepted: 10 February 2024  
© The Author(s) 2024

## Abstract

In recent years, additive manufacturing (AM) techniques have gained increased attention. The most common AM technologies to realize complex parts are powder bed-based fusion processes, especially electron beam powder bed fusion of metals (PBF-EB/M) and laser-based powder bed fusion of metals (PBF-LB/M). Focusing on industrial applications, cyclic loading scenarios and fatigue properties of components produced by such techniques came into focus of research. The present work deals with a comparison between microstructure, hardness, density and fatigue properties of a high-alloy tool steel AISI H13 (1.2344, X40CrMoV5-1) manufactured by PBF-EB/M and PBF-LB/M. The investigated specimens are characterized by a complex phase composition containing ferrite, perlite, bainite and martensite, eventually resulting in different hardness values depending on the used AM technology. Fatigue data for PBF-EB/M AISI H13 are reported for the first time in open literature. It is shown that the fatigue behavior is significantly influenced by the specimen density. Accordingly, parts with a high density are characterized by superior fatigue strength.

**Keywords** Additive manufacturing (AM) · Electron beam melting (EBM) · PBF-EB/M · Selective laser melting (SLM) · PBF-LB/M · X40CrMoV5-1 (H13) · Microstructure · Cyclic load · Bainite

## 1 Introduction

Additive manufacturing (AM) of high-performance steels is highly interesting for the tooling industry. Due to the high design freedom, complex structures like conformal cooling channels can be manufactured without raising the cost of the AM component [1, 2]. For example, they can be used in sliders for die-casting applications and reduce hot spots by cooling close to the contour, thus increasing durability

and reducing costs [3, 4]. Powder bed-based processes represent the most common AM technologies for metallic materials [5, 6]. They are separated based on the energy source used, i.e., electron beam powder bed fusion of metals (PBF-EB/M), also known as electron beam melting (EBM), and laser-based powder bed fusion of metals (PBF-LB/M), also known as selective laser melting (SLM). Both technologies are characterized by a layerwise fabrication principle. Highly dense parts can be obtained being characterized by mechanical properties similar to conventionally manufactured counterparts [1, 7]. In particular, both processes are based on a cyclic repetition of depositing powder, selective melting of the powder and lowering the build platform by a specific layer size. Besides the similarities, both technologies exhibit significant differences and requirements due to the different energy sources used. While the PBF-EB/M process is carried out under vacuum condition, shielding gases, such as Argon, are used in PBF-LB/M to avoid contamination and oxidation of powder feedstock and melt [8]. The PBF-EB/M process is further characterized by heating of the substrate plate and sintering of powder to prevent powder blasting. This eventually results in elevated process

---

✉ M. Kahlert  
kahlert@uni-kassel.de  
M. Vollmer  
vollmer@uni-kassel.de  
T. Wegener  
t.wegener@uni-kassel.de  
T. Niendorf  
niendorf@uni-kassel.de

<sup>1</sup> Institute of Materials Engineering - Metallic Materials, University of Kassel, Moenchebergstr. 3, 34125 Kassel, Germany

temperatures [6]. However, the final density of components manufactured by powder bed-based processes depends on a combination of specific process parameters including, for example, the power of the energy source, scan speed and hatch distance [9]. Especially in PBF-LB/M, a constant gas flow is necessary to obtain dense parts, since otherwise vaporization during melting of the powder can affect the laser beam, eventually resulting in an insufficient energy input in the material, and thus, a low depth of the melt pool and lack of fusion defects (LoF).

AISI H13 (1.2344, X40CrMoV5-1), solely referred to as H13 in the remainder of this manuscript, represents a well-known tool steel that is commonly used in the manufacturing industry for a wide range of applications. As H13 is characterized by good resistance to thermal softening and wear, high hardenability, high strength, high thermal conductivity and excellent toughness this tool steel is the material of choice for different types of hot working dies, such as forging dies, extrusion dies, and die-casting dies [10–12]. Caused by carbide-forming elements, the hardness of the steel is stabilized up to temperatures of about 500 °C [13]. As a result, a high ultimate strength and wear performance is guaranteed to prevent an early failure in application [9, 13, 14]. Up to now, H13 was manufactured by many different AM technologies. Bajaj et al. [15] give an overview of the different investigations found in open literature. The microstructure of H13 manufactured by PBF-LB/M is reported to consist of a mixture of martensite, retained austenite in the interdendritic regions as well as carbides [9, 16]. The resulting mechanical properties strongly depend on the substrate temperature. At 200 °C, the specimens show a hardness of  $706 \pm 147$  HV resulting in an ultimate tensile strength of  $1620 \pm 215$  MPa [17]. Due to a high cooling rate up to  $10^6$  Ks<sup>-1</sup> in PBF-LB/M, cracking occurs below a critical substrate temperature of about 170 °C as a result of residual stresses [9, 18]. However, apart from cracking other types of defects can also appear during processing of H13 via PBF-LB/M. Wu et al. [9] report on defects resulting from different powder batch qualities as well as solidification cracks, which are induced by chemical inhomogeneity. In contrast to PBF-LB/M, only a few studies investigating the processing of H13 via PBF-EB/M are available in open literature. Some years ago, Cormier et al. [19] and Rännar et al. [20] investigated the processability and a use case for PBF-EB/M manufactured H13. Moreover, in a recent study, the microstructure and mechanical properties of PBF-EB/M processed H13 were studied in detail by some of the present authors [21]. It was shown that a fine-grained microstructure revealing a mixture of martensite and bainite with carbides and a low content of retained austenite prevails, resulting in quasi-static mechanical properties similar to conventionally manufactured H13 counterparts. The specimens processed by PBF-EB/M additionally

exhibit a hardness of approximately 510 HV resulting in a maximum ultimate tensile strength of 1796 MPa [21]. These results are in good agreement with investigations made on AISI H11 (X37CrMoV-1) processed by PBF-EB/M being characterized by similar microstructural and mechanical properties [22].

In recent years, industrial applications using AM techniques increased rapidly [23, 24]. As a result, fatigue properties came into focus of research and industry. In general, fatigue represents a proceeding and localized structural damage that occurs, when technical parts are subjected to cyclic loading. In most cases, fatigue failure starts with crack initiation at notches, i.e., due to an increased surface roughness or internal pores. Such features eventually promote local stress maxima [25, 26]. In AM parts, the most critical defects concerning fatigue are LoF pores in direct vicinity of the surface [27, 28]. However, also AM parts with a high density often show inferior fatigue strength as compared to conventional counterparts caused by a high surface roughness and internal stress [10]. Even in case of machined specimens, the fatigue strength is often significantly lower than the strength of conventional parts. In case of high internal stress, the fatigue strength can be significantly improved by a stress relieving heat treatment [10, 27]. In this context, Mazur et al. [10] were able to increase the fatigue strength of a H13 steel from below 100 MPa in the PBF-LB/M as-built condition to about 250 MPa for a stress relieved condition. However, it should be noted that conventionally manufactured and heat treated specimens (520 HV) reached a fatigue strength of 750 MPa [10]. Further studies [28, 29] on the other hand reported a fatigue strength of conventionally cast H13 of less than 400 MPa. Dörfert et al. [27] found out that surface machining can increase the fatigue strength of PBF-LB/M specimens, however, final properties remained inferior due to residual porosity of the AM parts. In addition, Pellizzari et al. [28] elaborated that for increasing the fatigue strength, the residual porosity has to be minimized in terms of number and size. In case LoF defects are present, the final performance highly depends on the load direction with respect to the build direction due to the anisotropic shape of LoF defects [28]. In a recent study, Garcias et al. [30] compared the fatigue strength of conventionally and PBF-LB/M processed H13. The authors reported on LoF defects (8%) significantly lowering the fatigue strength of the PBF-LB/M specimens to 38 MPa [30]. Macek et al. [31] analyzed the fracture behavior of H13 fatigue specimens. The authors identified transgranular fracture as the predominant failure mechanism. However, investigations on the fatigue behavior of PBF-LB/M H13 are still limited and only difficult to compare reasoned in different specimen geometries and fatigue parameters. Data reporting on the fatigue properties of PBF-EB/M processed H13 have not been reported so

far. In recent years, even data driven and machine learning approaches, respectively, were applied in studies focusing on AM process development [32–34]. However, to apply such models, it is important to have an adequate data base for training. The present study was conducted to contribute to the elaboration of such data.

In order to close the prevalent research gaps elaborated above, the present study compares the fatigue behavior of H13 manufactured by PBF-EB/M and PBF-LB/M. The prevailing microstructure after processing was analyzed by optical microscopy (OM) and electron backscatter diffraction (EBSD) measurements. In addition, hardness distribution was studied based on Vickers hardness mappings. The fatigue behavior was investigated under fully reversed push–pull loading ( $R_\sigma = -1$ ). Finally, fracture surface analysis allowed to examine the failure evolution. From the results presented, process-microstructure-fatigue property relationships were deduced.

## 2 Materials and methods

In the present study, two powder bed fusion (PBF) machines were used for processing: An A2X machine from Arcam AB for PBF-EB/M and a SLM 280HL system from SLM Solutions AG for PBF-LB/M. The Arcam A2X has a maximum power of 3000 W and is able to realize substrate temperatures up to above 1000 °C. In the build chamber, a controlled vacuum is applied using a light helium atmosphere in order to increase the electrical conductivity during the process. The laser of the SLM 280HL used in the present investigation is characterized by a maximum power of 400 W and a Gaussian profile. For suppressing oxidation processes, Argon was used as shielding gas in the build chamber. In both machines, the same H13 powder was used being characterized by a particle size range between 45 and 106  $\mu\text{m}$ . The powder was gas-atomized by m4p material solutions GmbH and had a nominal chemical composition of 0.4% C, 5.3% Cr, 1.4% Mo, 1% V (wt.%) balanced with Fe. In both PBF processes, cuboids with 10 mm length, 10 mm width and 40 mm height were built using a bidirectional scanning strategy with 90° rotation between the layers and without using a contour scan and support structures. For improved vapor removal in the PBF-LB/M process, the cuboids were manufactured with an angle of 45° to the gas flow direction (15 m/s). In both processes, the cuboids were built on an austenitic stainless steel substrate plate. The nominal temperature of the respective substrate plate (150 × 150 × 10 mm) was 900 °C in the PBF-EB/M and 200 °C in the PBF-LB/M process ( $\varnothing$  90 × 20 mm). In order to ensure a sufficient electrical conductivity of the powder during PBF-EB/M, the temperature of 900 °C was held for

10 min before the build job was started. For pre-sintering and heating a power of 2400 W, a velocity of 13,000 mm/s and a hatch distance of 1 mm were used. In order to realize the target temperature of 900 °C, the pre-sintering was repeated 20–23 times each layer. For the melting process, parameters applied in a previous study [21] were optimized in a preliminary test to increase production efficiency (by increasing the hatch distance and power at similar volume energies). The PBF-EB/M parameters resulting in the highest density were then applied in the present study and are listed in Table 1. For PBF-LB/M process parameters based on a previous study [9] were used and are also listed in Table 1. After processing, the cuboids were analyzed using Optical Emission Spectroscopy (OES). The chemical compositions determined revealed 0.32% C, 5.24% Cr, 1.7% Mo, 1.2% V balanced with Fe after the PBF-EB/M process as well as 0.3% C, 5.25% Cr, 1.7% Mo, 1.18% V balanced with Fe after the PBF-LB/M process.

For microstructural and mechanical characterization, flat dog-bone shaped specimens were cut by electro-discharge machining (EDM) from the above-mentioned cuboids. The overall dimensions of the specimens are shown in Fig. 5. The specimen geometry was numerously used in literature (e.g., in [21, 35, 36]), however, has not been captured by an official standard, yet. Microstructural analysis was carried out on specimens being mechanically ground down to 5  $\mu\text{m}$  grit size and subsequently vibro-polished with OP-S Non-Dry from Struers for at least 18 h. For OM, the specimens were etched using Adler Solution (100 cm<sup>3</sup> H<sub>2</sub>O, 200 cm<sup>3</sup> HCl, 60 g FeCl<sub>3</sub>, 12 g (NH<sub>4</sub>)<sub>2</sub>[CuCl<sub>4</sub>]) for 1 s and subsequently analyzed using a Keyence VHX-7000. For nanoindentation analysis of the etched specimen a nanoindentation tester NHT3 from Anton Paar GmbH was used. The maximum load applied was 10 mN with a loading rate of 20 mN/min and a pause of 10 s between loading and unloading. Further microstructural characterization was carried out using a Zeiss ULTRA GEMINI high-resolution scanning electron microscope (SEM) equipped with a QUANTAX EBSD unit from Bruker Corporation. During EBSD measurements the SEM was operated at an acceleration voltage of 20 kV with a working distance of 14 mm and a step size of 0.3  $\mu\text{m}$ . For hardness measurements, specimens were

**Table 1** Parameter sets used for PBF-EB/M and PBF-LB/M processing

	Power, W	Velocity, mm/s	Hatch distance, mm	Layer thickness, $\mu\text{m}$	Volume energy, J/mm <sup>3</sup>
PBF-EB/M	600	3000	0.1	50	40
PBF-LB/M	400	800	0.1	50	100

polished to 5  $\mu\text{m}$  grit size. A Durascan 70 testing system from Struers GmbH was used. For both conditions, a matrix with 383 indents (HV 0.5) covering the entire specimen surface was recorded. The average hardness values were calculated from all indents of each mapping. For mechanical characterization, i.e., fatigue testing, the specimens were polished to 5  $\mu\text{m}$  grit size in order to avoid any influence of roughness on the fatigue results. The fatigue tests were conducted using a digitally controlled servo-hydraulic load frame with a maximum force capacity of 16 kN in force control at 10 Hz in fully reversed push-pull loading ( $R_\sigma = -1$ ). The specimen temperature was measured continuously in order to avoid testing temperatures being above 30  $^\circ\text{C}$ . For determination of the fatigue strength, the loading stress was lowered by 50% after failure of a specimen starting at the yield strength of about 900 MPa as reported in a previous study [21]. The maximum number of cycles for fatigue testing was set to  $2 \times 10^6$ . If specimens reached this number of cycles without failure, they were defined as runouts and the loading stress was increased by 50% in the following test. To ensure reproducibility and to investigate the scatter behavior, at least three specimens were tested at each stress level. However, the investigations are not based on an official standard. Fracture surface investigations after fatigue testing were conducted using the Zeiss ULTRA GEMINI high-resolution SEM detailed above. During fracture surface analysis, the SEM was operated at 20 kV, the working distance was set to 25 mm. A flowchart summarizing the experimental flow of the present study as described above is depicted in Fig. 1.

### 3 Results and discussion

The processability of H13 using PBF-EB/M was previously demonstrated by the group of the current authors [21]. Specimens built using suitable process parameters show a very high density (cf. Fig. 2a) resulting in mechanical properties similar to conventionally produced material. On the contrary, many challenges are reported upon using PBF-LB/M for processing of high carbon steels. For example, Wu et al.

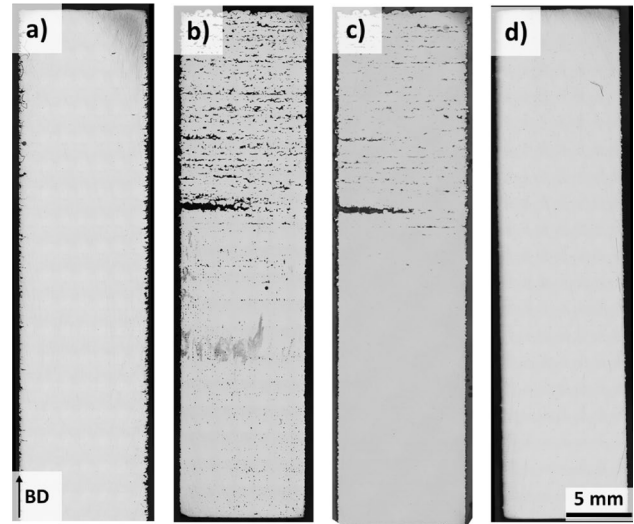


**Fig. 2** Optical micrographs of the cuboid blocks, where fatigue specimens were cut from by EDM. Fully dense specimens processed by a PBF-EB/M and d PBF-LB/M; b and c reveal a high porosity in PBF-LB/M specimens resulting from vaporization

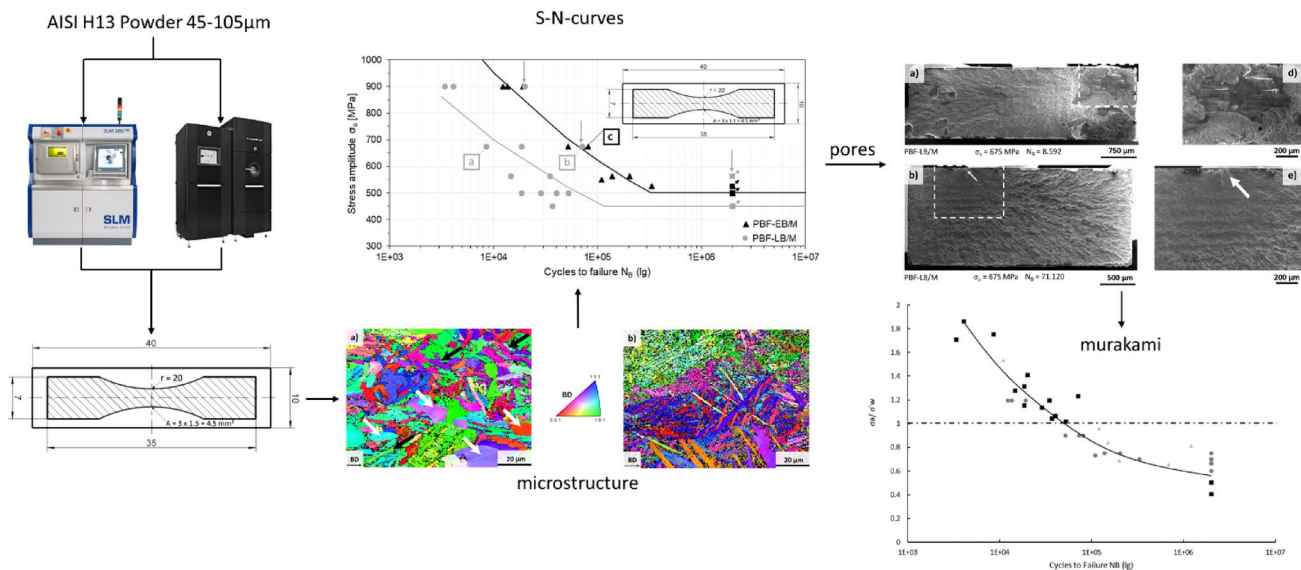


**Fig. 1** Flowchart explaining the experiment flow of the present study



[9] revealed an influence of different powder batches due to slightly different carbon contents, eventually resulting in differences in the cracking behavior of the built components. The authors also investigated the influence of different laser settings. When the energy input is too low to melt the powder sufficiently, the powder remains unmolten, and thus, significantly deteriorates the mechanical properties. In contrast, a high energy input promotes the formation of hot cracks and keyholes. To avoid the influence of different powder batches and different carbon contents, respectively, the authors of the present study used one powder batch for PBF-LB/M and PBF-EB/M. As a result, a relatively high laser power was applied in the PBF-LB/M process to sufficiently melt the powder being characterized by a distribution of 45–105  $\mu\text{m}$ . By using a high laser power, an intense vaporization of elements can occur, shadowing the laser beam and resulting in LoF defects. Preliminary investigations carried out by the authors of the present study have shown that the vaporization can be reduced by an optimization of the scan path relative to the gas flow as well as by reducing the layer thickness and the energy input (data not shown). Here, it has to be pointed out that the powder used for PBF-LB/M contains particles being larger than commonly applied in this process. This may further contribute to the evolution of defects; however, the shadowing effects are thought to be the main issue in present work. Due to the process parameters applied in PBF-LB/M, most importantly the layer thickness and the coating parameters, no detrimental effect of the powder particle size used was seen. In contrast, the vaporization effect can be deliberately used to produce parts being characterized by wide-ranging differences in the resulting density in one single build job. These effects were used to produce parts with different densities (cf. Fig. 2b–d) in order to investigate the influence of pore size on the fatigue behavior and to compare them with parts of high density produced via PBF-EB/M. In the following, the entire data base is shown for a complete discussion on the impacts of porosity, microstructure, hardness and fatigue behavior.

In order to characterize the prevailing microstructure of the H13 components manufactured by PBF-EB/M and PBF-LB/M, respectively, Fig. 3 shows optical micrographs of etched specimens of both conditions. The specimen processed by PBF-EB/M (Fig. 3a) is characterized by the concomitant appearance of brighter and darker areas with a size of approximately 20  $\mu\text{m}$ , which are marked by arrows. After etching using the Adler Solution, areas with low carbon content appear brighter than areas with high carbon content [37, 38]. Thus, the brighter areas seen can be either ferrite or blocky martensite. Some of the present authors assessed the cooling path in case of PBF-EB/M processed H13 based on analysis of a conventional continuous cooling transformation (CCT) phase diagram [21]. The predominant phases according to the CCT are perlite, bainite and martensite, whereas

ferrite should not be present. Thus, it is expected that the bright areas consist of blocky martensite and, thus, these are labeled with M (cf. Fig. 3a). To confirm this assumption, nanoindentation tests were carried out revealing highest nano-hardness values (12 GPa) for these specific areas. The high nano-hardness is in line with the investigation of Hearn et al. [39]. Within that study the authors were able to show a high nano-hardness in martensitic areas in an AM manufactured 0.45-C steel. An in-depth discussion of the hardness will be provided in a following section of this chapter. The areas, which appear darker, are characterized by a higher amount of carbon and can be identified as perlite (arrow marked with P in Fig. 3a). Nanoindentation tests in this area revealed hardness values of about 3.5 GPa. In addition, needle-like structures characterized by internal gray pattern can be observed. In general, such gray pattern can be seen when diffusion of small amounts of carbon occurs, which is the case during bainitic phase transformation caused by a medium cooling rate [38]. This kind of needles have also been observed in a study by Keul et al. [40], who investigated the influence of the chromium content on the resulting microstructure in bainitic forging steels. In that study, a shifting of the bainitic start temperature to lower temperatures by increasing the chromium content was reported. In the present work, these needle-like structures are also classified as bainite (arrow marked with B in Fig. 3a) being characterized by a nano-hardness of approximately 6 GPa. In contrast, the microstructure of a specimen processed by PBF-LB/M is shown in Fig. 3b. This condition is characterized by a fine needle-like structure. Moreover, sizes of microstructural features are significantly smaller compared to the PBF-EB/M condition resulting in a nano-hardness up to 12 GPa. These differences in the microstructures between PBF-EB/M and PBF-LB/M can be explained by the different time–temperature-paths of both processes, which are illustrated in Fig. 3c and d. While the material in PBF-LB/M featuring a relatively low build-plate temperature cools down very quickly from liquid to temperatures below martensite start temperature ( $M_s$  of about 300 °C [41]), the PBF-EB/M process is characterized by a steady process temperature of about 900 °C and a cooling down from this temperature only at the end of the process. Here the cooling rate is slow, which likely promotes the formation of bainite. Due to the higher cooling rate during PBF-LB/M (as compared to PBF-EB/M), it is thought that the fine needle-like structures (cf. Fig. 3b) are martensite (arrow marked with M). In contrast to the PBF-EB/M condition, the black and white ratio here is likely related to a different topography of the martensitic needles and therefore a different light reflection in the OM image. This assumption is supported by Bajaj et al. [15], who reported that a martensitic structure is the typical microstructure appearing in PBF-LB/M processed tool steels.

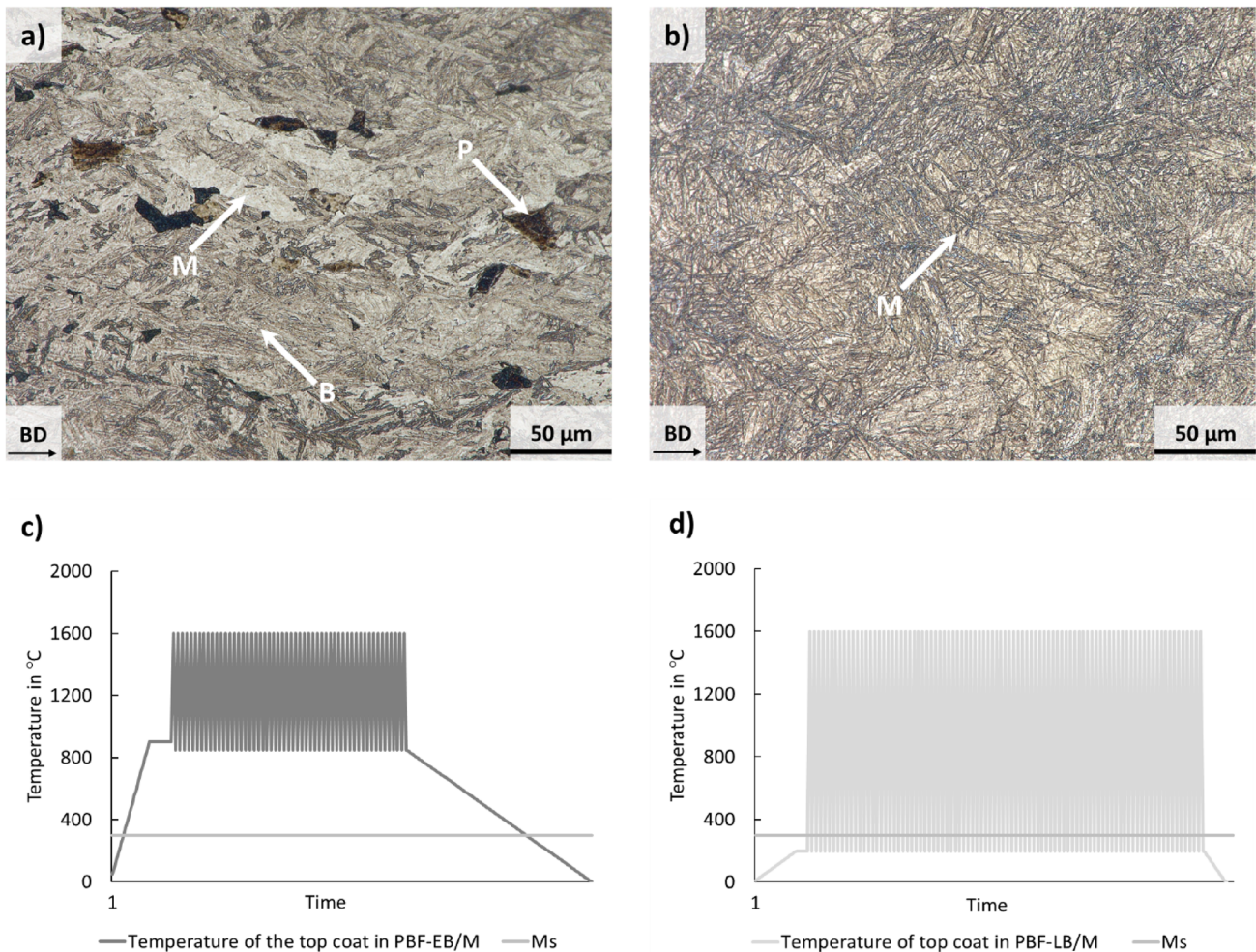


**Fig. 3** Representative optical micrographs of H13 processed by **a** PBF-EB/M and **b** PBF-LB/M. The specimens were etched using Adler Solution for 1 s. The build direction (BD) is highlighted in the

lower left corner. Schematics of the time temperature paths in the current top layer are shown for PBF-EB/M in **c** and for PBF-LB/M in **d**, respectively

Figure 4 shows representative EBSD inverse pole figure (IPF) maps for both PBF processes considered. Generally, these IPF maps confirm the needle-like microstructure already highlighted in Fig. 3. The corresponding phase maps (PM) of both conditions are additionally shown in Fig. 4c and d, revealing a mainly body centered cubic (bcc) phase structure with a smaller amount of embedded face centered cubic (fcc) phase. However, a higher amount of fcc phase in the PBF-LB/M condition can be seen, which can be classified as retained austenite. This finding is in line with the investigations of Krell et al. [16]. In their investigation on PBF-LB/M processed H13, the authors reported a network like honeycomb structure of retained austenite with a volume fraction of 20–25%. Obviously, the specimen processed by PBF-EB/M (Fig. 4a) shows a high amount of oval-shaped grains (white arrows) in addition to the needle-like structures (black arrows), which are slightly elongated in build

direction with dimensions of approximately 5 to 50 μm. In previous studies reporting on H13 processed by PBF-EB/M, a mixed microstructure consisting of ferrite with carbides (perlite), bainite, martensite and retained austenite was found [19, 21]. The process inherent medium cooling rate already mentioned above, which is characteristic for PBF-EB/M (the build volume cools down in its entirety after melting the uppermost layer) [21], and the bcc structure of the oval-shaped grains in combination with the findings shown in Fig. 3 are strong indicators that the oval-shaped grains are formed by perlite. In contrast, the areas with a more needle-like morphology are characterized by a lower image quality. Bainite and martensite phases are known to be characterized by high dislocation density and distortions, respectively [42, 43]. As a result, such structures are more difficult to index in EBSD analysis. Thus, it is reasonable to conclude that the needle-like features are consisting of



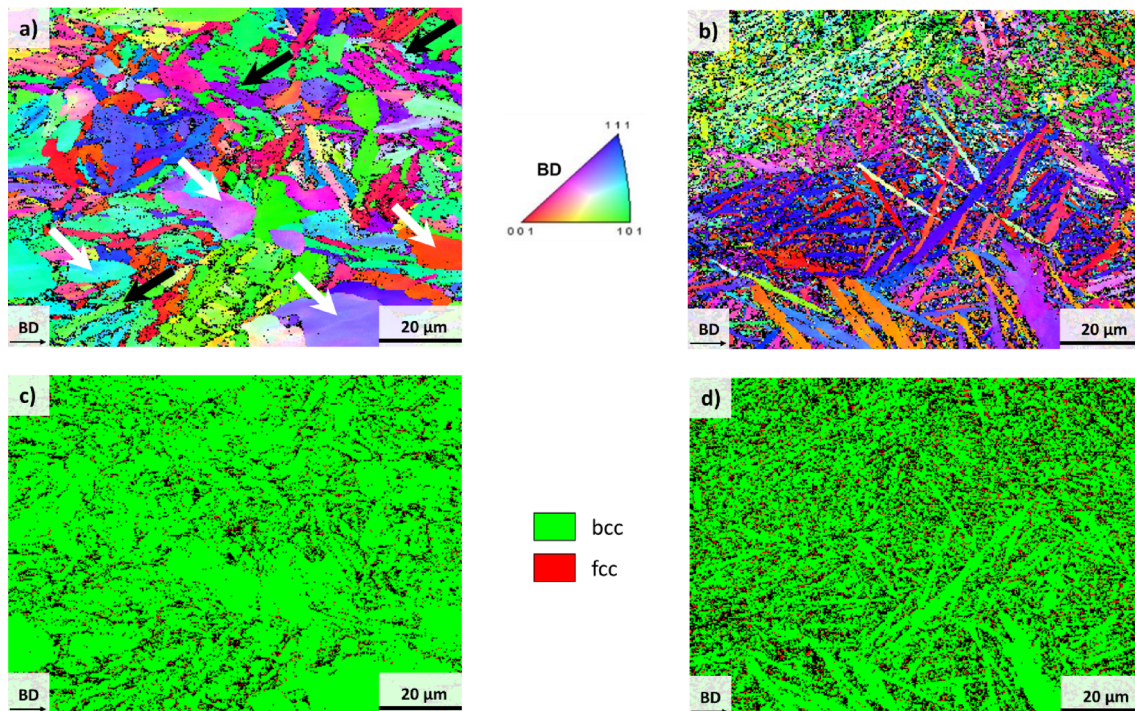


**Fig. 4** EBSD inverse pole figure (IPF) maps of H13 processed by **a** PBF-EB/M and **b** PBF-LB/M. The grain orientations are plotted with respect to the build direction indicated by the arrow in the lower left marked with BD; **c** and **d** show the corresponding phase maps (PM)

bainite and martensite. In contrast, the IPF map of the PBF-LB/M specimen is shown in Fig. 4b. The microstructure obtained appears to be significantly more needle-like as compared to the microstructure of the PBF-EB/M specimen. This can be rationalized by a higher volume fraction of martensite. Moreover, no areas being free of needle-shape features can be found indicating the absence of perlite. Similar microstructures for PBF-LB/M manufactured H13 were found by various authors [9, 15, 16] and were explained by the high cooling rates prevailing during PBF-LB/M processing [18]. Rapid cooling eventually promotes the formation of a martensitic phase structure accompanied by retained austenite. A preferred crystallographic direction cannot be seen for both conditions.

The results of the hardness measurements are presented by hardness maps as shown in Fig. 5. For PBF-EB/M, an average hardness of  $471 \pm 36$  HV0.5 was obtained. As already discussed in [21], the hardness increases with increasing build height of the specimen. This can be rationalized by a higher cooling rate in the upper layers of the specimen as well as annealing effects influencing the lower areas. In comparison, the PBF-LB/M specimen is characterized by a more homogeneous hardness distribution with respect to the build height as can obviously be deduced from the hardness map in Fig. 5. The calculated average hardness of  $697 \pm 21$  HV0.5 has a significant higher level compared to the hardness of the PBF-EB/M counterpart specimen. As

detailed before, this can be rationalized by the higher cooling rate prevailing in the entire volume of the PBF-LB/M specimen compared to the PBF-EB/M specimen eventually leading to different microstructures. The higher cooling rate is reasoned by the lower substrate temperatures in PBF-LB/M compared to PBF-EB/M (cf. Fig. 3c and d). The hardness found in both conditions is in line with hardness values reported in literature for PBF processed H13 [9, 15, 17, 21].

Figure 6 shows Woehler-type S–N curves of both PBF conditions considered. It is obvious, that the PBF-EB/M condition is characterized by superior fatigue properties as compared to the PBF-LB/M processed counterparts. Irrespective of the stress level considered, the average fatigue life of the PBF-EB/M condition is increased by a factor of approximately 1.5 to 2. From the results presented, fatigue strengths of 500 MPa and 450 MPa can be determined for the PBF-EB/M and PBF-LB/M condition, respectively. However, it has to be noted that these values are not based on statistical evaluation. Up to now, fatigue strength of PBF processed H13 was only discussed for PBF-LB/M in open literature. Mazur et al. [10] reported on the fatigue strength of various H13 conditions. The PBF-LB/M specimens (based on the relevant standards ASTM E8 and ASTM E466) were fatigued with as-build surfaces leading to a fatigue strength of 100 MPa at  $2 \times 10^6$  cycles in fully reversed push–pull loading ( $R = -1$ ). In contrast, a condition

**Fig. 5** Hardness maps of specimen processed by PBF-EB/M and PBF-LB/M. The BD of the specimens shown in the maps is indicated by the arrow “BD” and the average hardness is labeled “AH”. It has to be noted that different scale bars were used for both hardness maps for clarity

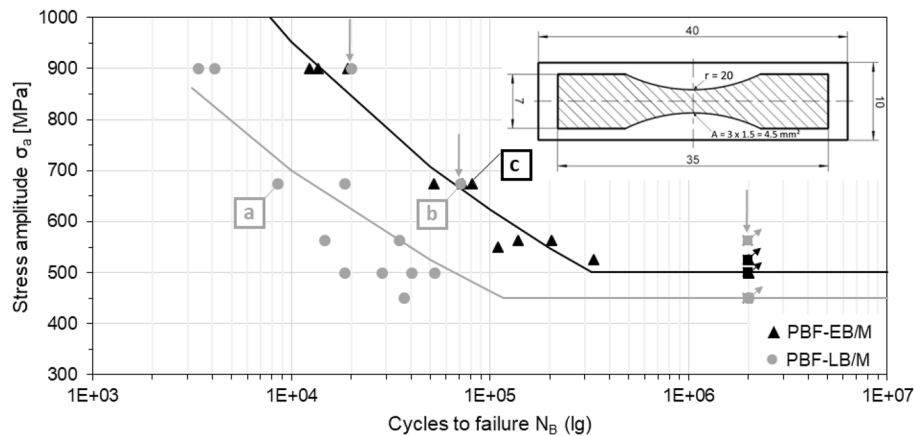
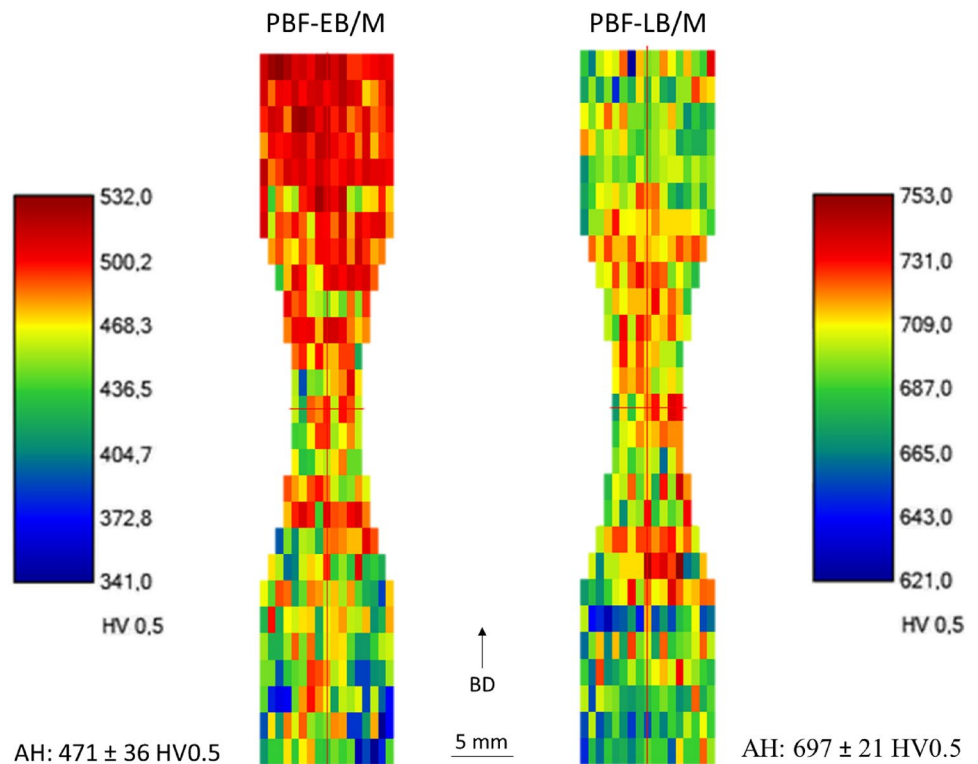


**Fig. 6** Woehler type S–N diagram ( $R_{\sigma} = -1$ ) of specimens processed by PBF-EB/M and PBF-LB/M. The geometry of the fatigue specimens wire-cut by EDM from the manufactured 10 mm × 10 mm × 40 mm cuboids is displayed in the upper right corner.

being characterized by an as-build surface subjected to an additional stress relieving heat treatment showed a fatigue strength of 300 MPa at  $2 \times 10^6$  cycles [10]. Moreover, a conventionally processed and heat treated H13 condition was investigated revealing a fatigue strength of 850 MPa at  $2 \times 10^6$  cycles [10]. In direct comparison to these results, it can be concluded that the fatigue strength of the specimens studied in the present work is on a significantly higher level compared to the AM specimens investigated by Mazur et al.

ner. PBF-LB/M specimens wire-cut out of one cuboid showing highest relative density are marked with an arrow. The PBF-LB/M specimen further studied by fractography (results displayed in Fig. 7) are highlighted by a, b, c

[10]. However, due to the different initial surface conditions and the higher porosity, the results are difficult to compare.

Taking into account the average hardness value of the PBF-LB/M condition (697 HV, cf. Fig. 5) compared to the PBF-EB/M counterpart (470.5 HV, cf. Fig. 5), different tendencies would have been expected regarding fatigue strength as a higher hardness usually indicates a higher fatigue strength [44]. However, the results displayed in Fig. 6 clearly highlight significant differences with respect

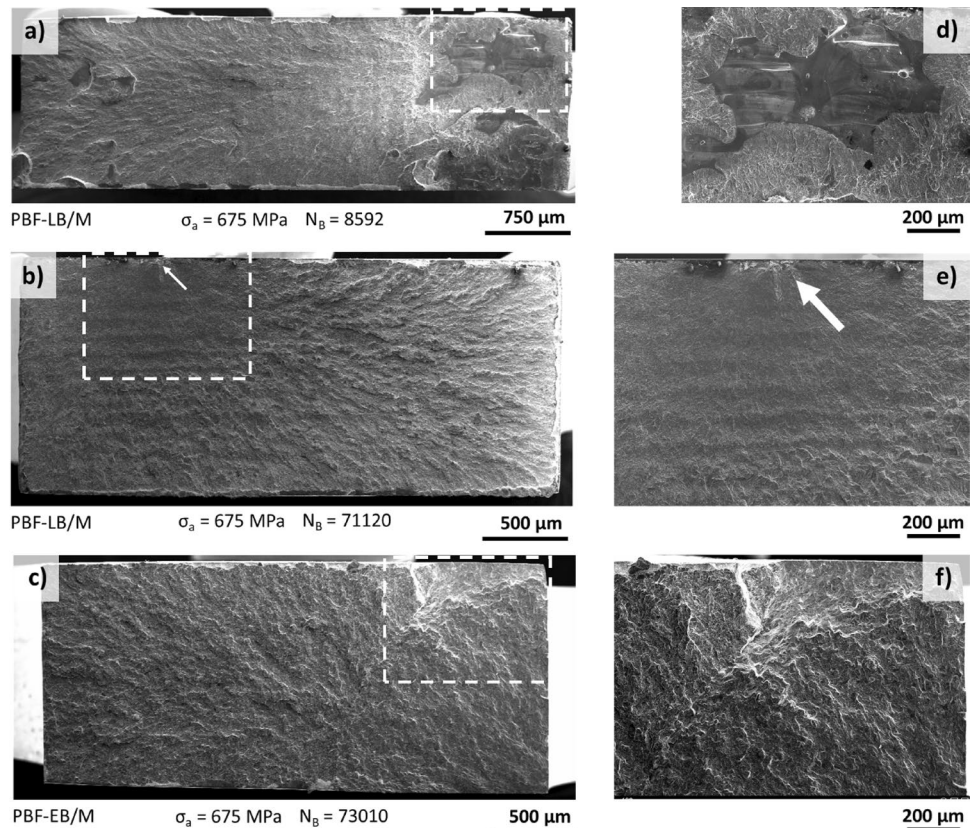


to scatter at first glance. While the PBF-EB/M condition is characterized by a high reproducibility, the PBF-LB/M condition reveals pronounced scatter in the data obtained. This observation is particularly underlined by a runout specimen of the PBF-LB/M condition fatigued at a stress amplitude of 550 MPa, which is well above the approximated fatigue strength of the PBF-EB/M condition. At this point, it has to be noted that all superior specimens processed by PBF-LB/M, i.e., being characterized by an increased number of cycles to failure (marked by the gray arrows in Fig. 6), were cut from one cuboid being characterized by highest relative density (cf. Fig. 2d).

In order to shed light on the mechanisms being responsible for the results obtained by fatigue testing, fracture surface analysis was carried out. The corresponding results are shown in Fig. 7. The secondary electron (SE) contrast images were taken from the fracture surfaces of PBF-EB/M and PBF-LB/M specimens marked by (a)–(c) in Fig. 6. All specimens were tested using the same stress amplitude of 675 MPa. The PBF-LB/M specimen shown in Fig. 7a reveals a high number of LoF defects on the fracture surface, resulting in multiple crack initiation sites and, thus, a significant lower number of cycles to failure ( $N_B = 8.592$  cycles) as compared to the other PBF-LB/M specimen shown in Fig. 7b ( $N_B = 71.120$  cycles). Process-induced defects are well-known to lead to pronounced

scatter in fatigue life. This can be rationalized by a scattering of defects in critical areas in direct vicinity of the specimen surfaces. Pellizzari et al. [28] were able to pinpoint pores located in direct vicinity of the surface as most critical points for fatigue fracture in their specimens. In contrast to the fracture surface shown in Fig. 7a, hardly any large defects can be observed on the fracture surface of the PBF-LB/M specimen shown in Fig. 7b. It can be deduced that the low defect density in this specific specimen leads to the increased number of cycles to failure (by a factor of more than eight). Still, fatigue crack initiation takes place in the direct vicinity of the surface, with the crack starting defect marked by an arrow and highlighted in the magnified view in Fig. 7e. Under cyclic loading such defects act as local stress raisers [45]. Similar to the PBF-LB/M specimen shown in Fig. 7b, the PBF-EB/M specimen (Fig. 7c) does not reveal any process induced defects on the fracture surface (also at higher magnification shown in Fig. 7f no defects can be observed). Moreover, based on investigations of all fracture surfaces of the PBF-EB/M condition, process induced defects were not found in any specimen (data not shown for the sake of brevity). Therefore, it is likely that the PBF-EB/M process is more resistant to the appearance of defects, eventually resulting in a less pronounced scattering of cycles to failure.

**Fig. 7** SEM micrographs of representative fracture surfaces for selected specimens fabricated by PBF-LB/M in **a** and **b** and PBF-EB/M in **c** after fatigue at a stress amplitude of  $\sigma_a = 675$  MPa. Respective specimens are labeled **a–c** in Fig. 6



In the field of fatigue life prediction of defect-based materials, the Murakami model [46] can be used to estimate the fatigue strength  $\sigma'_w$  based on the empirical correlation of the macro-hardness and crack-initiating defect size with the threshold value of the stress intensity factor  $\Delta K_{th}$ . For an in-depth analysis of the impact of pores on scatter and fatigue life, the stress amplitudes used in the fatigue tests of the present study were thus standardized using the Murakami fatigue limit  $\sigma'_w$  calculated based on the area of the critical defect in each specimen [47]. The formula used to calculate the individual Murakami fatigue limits  $\sigma'_w$  is shown in Eq. (1), where HV is the average Vickers hardness of the specimens (as calculated from the hardness maps, cf. Fig. 5), C is a location dependent constant between 1.43 for pores located in direct vicinity of the surface and 1.56 for defects located in the inside of the cross section, and the  $\sqrt{\text{area}}$  parameter is the representative defect size, which is defined by the square root of the area obtained by a circle covering the critical defect. For specimens revealing no pores on the fracture surface, as well as for runout specimens, the Murakami fatigue estimation of  $1.6 \times HV$  was used [47, 48]. According to the Murakami model, the fatigue strength is achieved at high and very high numbers of cycles if the condition-specific threshold value  $\Delta K_{th}$  as a function of defect size and macro-hardness is undercut [46]. Table 2 lists the parameters applied as well as the calculated Murakami fatigue limits for all fatigue specimens investigated in the present study.

$$\sigma'_w = \frac{C(HV + 120)}{\sqrt{\text{area}}^{1/6}} \quad (1)$$

Figure 8 shows the ratio of the experimentally tested stress amplitude ( $\sigma_a$ ) and the individual Murakami fatigue limits ( $\sigma'_w$ ) plotted against the number of cycles to failure ( $N_B$ ) for the specimens fatigued in the present study and also for specimens reported in literature, where data were recompiled from Pellizzari et al. [28]. It is obvious that the scatter is significantly reduced, independent of the considered data. Moreover, independent of the process used for AM, i.e., PBF-LB/M and PBF-EB/M, nearly the same S–N curves can be derived. The significantly reduced scatter can be clearly attributed to the virtually reduced influence of the porosity, since the critical pores leading to defect initiation are inherently considered by the Murakami fatigue limit. In case a large defect is present, the Murakami fatigue limit is minimized and, thus, the ratio of the tested stress amplitude ( $\sigma_a$ ) and the Murakami fatigue limit ( $\sigma'_w$ ) increases. Vice versa, if the defect is small, the ratio decreases. Murakami et al. [48] further mentioned other factors that can influence scatter, e.g., the microstructure or a poor alignment of testing machine and specimens. However, such factors would not lead to the reduced scatter of the standardized S–N curve

and the data recompiled from Pellizzari et al. [28] would not be in line with the data of the present study. The converging curves of the PBF-LB/M and PBF-EB/M specimens can be rationalized taking into account the different hardness values after processing. Although no critical defects were observed in the investigated PBF-EB/M specimens, the condition is characterized by a much lower hardness compared to the PBF-LB/M condition and, thus, shows a lower Murakami fatigue limit. Also, the potential influences of the specimen geometry applied should always be taken into account. However, by comparing the data of the present study with the data of Pellizzari et al. [28], the Murakami approach in Fig. 8 clearly reveals that the results of both studies are in good agreement, despite the fact that Pellizzari et al. [28] used specimens that are more like the standard. This demonstrates that the fatigue properties are clearly dominantly influenced by defects in contrast to the specimen geometry.

Considering the runouts ( $N_B = 2 \times 10^6$ ) it can be seen that the estimated Murakami fatigue limit of  $1.6 \times HV$  is not met by the experimental data, eventually resulting in a quotient being lower than one. That means that the fatigue limit is overestimated based on the Vickers hardness, independent of the AM process used. Murakami et al. [47–49] already reported such kind of behavior, especially for low and medium carbon steels. They assumed that either high internal stress or microstructural inhomogeneities are responsible for the reduced fatigue limit. In the present study, a high impact of internal stress seems to be of lower importance as compared to microstructural inhomogeneities. Here, the time–temperature path of the PBF-EB/M process (cf. Fig. 3c) is known to result in very low internal stress [50]. Moreover, as shown in Fig. 3a and b, inhomogeneities in microstructure as well as needle-like structures, which are known to act as microstructural notches, are present in both conditions. Murakami et al. [49] discussed that such inhomogeneities can lead to many non-propagating cracks in low and medium carbon steels in case these are tested close to the fatigue limit. The characteristic fracture surface of the PBF-EB/M material shown in Fig. 7c and f confirms that a crack initiation point can be hardly identified. It seems that the crack interacts with the existing microstructure, which could be an indication for the emergence of several crack initiation points.

## 4 Conclusions

In the present study, AISI H13 specimens were successfully manufactured by means of electron beam and laser-based powder bed fusion of metals. Microstructural analysis in combination with fatigue tests revealed that the scatter in the number of cycles to failure strongly depends on the defect distribution, whereas microstructural differences mainly lead

**Table 2** Dataset for calculation of the Murakami fatigue limit

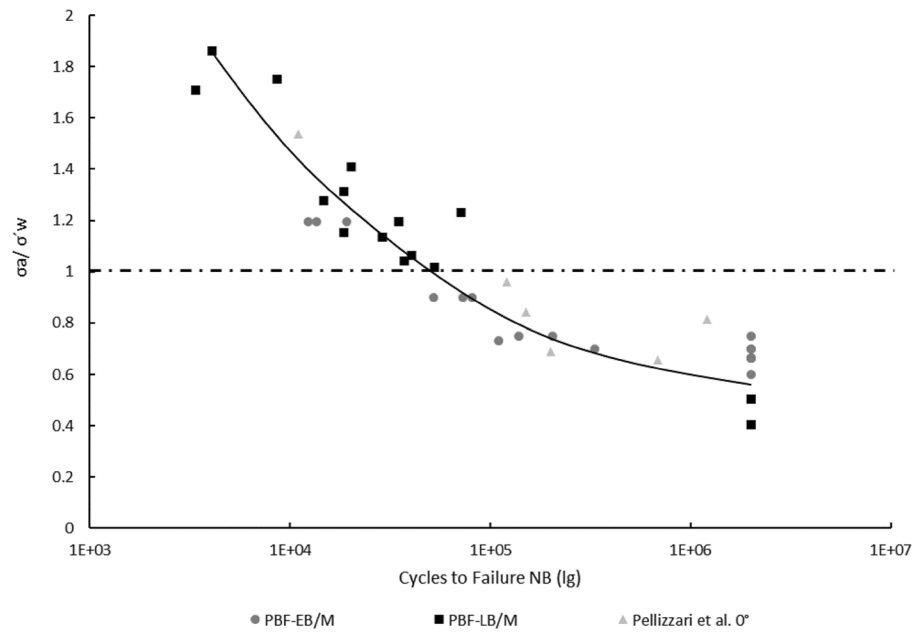
Process	Stress amplitude ( $\sigma_a$ ); MPa	Cycles to failure ( $N_B$ )	Critical pore diameter; $\mu\text{m}$	Location factor	$\sqrt{\text{area}}$ ; $\mu\text{m}$	Murakami fatigue limit ( $\sigma'_w$ ); MPA	$\sigma_a/\sigma'_w$	Hardness; HV
PBF-EB/M	450	2,000,000	n/a	n/a	n/a	752	0.60	470
	900	13,576	n/a	n/a	n/a	752	1.20	
	675	81,348	n/a	n/a	n/a	752	0.90	
	562.5	204,266	n/a	n/a	n/a	752	0.75	
	500	2,000,000	n/a	n/a	n/a	752	0.66	
	525	2,000,000	n/a	n/a	n/a	752	0.70	
	550	110,000	n/a	n/a	n/a	752	0.73	
	525	331,675	n/a	n/a	n/a	752	0.70	
	500	2,000,000	n/a	n/a	n/a	752	0.66	
	500	2,000,000	n/a	n/a	n/a	752	0.66	
	562.5	2,000,000	n/a	n/a	n/a	752	0.75	
	500	2,000,000	n/a	n/a	n/a	752	0.66	
	675	52,114	n/a	n/a	n/a	752	0.90	
	675	73,010	n/a	n/a	n/a	752	0.90	
	562.5	139,073	n/a	n/a	n/a	752	0.75	
	525	2,000,000	n/a	n/a	n/a	752	0.70	
	900	19,198	n/a	n/a	n/a	752	1.20	
	900	12,335	n/a	n/a	n/a	752	1.20	
PBF-LB/M	450	2,000,000	n/a	n/a	n/a	1115.2	0.40	697
	900	3398	227	1.56	201.17	526.52	1.71	
	675	18,663	154	1.43	136.48	514.89	1.31	
	500	52,903	202	1.43	179.02	492.12	1.02	
	500	18,622	430	1.43	381.08	433.90	1.15	
	450	37,159	446	1.43	395.26	431.27	1.04	
	450	2,000,000	n/a	n/a	n/a	1115.2	0.40	
	500	40,489	265	1.43	234.85	470.36	1.06	
	500	28,773	665	1.56	589.34	440.17	1.14	
	562.5	14,729	394	1.43	349.17	440.27	1.28	
	450	2,000,000	n/a	n/a	n/a	1115.2	0.40	
	900	4097	377	1.56	334.11	483.84	1.86	
	675	8592	875	1.43	775.45	385.45	1.75	
	562.5	35,103	265	1.43	234.85	470.36	1.20	
	900	20,112	42	1.43	37.22	639.38	1.41	
	562.5	2,000,000	n/a	n/a	n/a	1115.2	0.50	
	675	71,120	105	1.43	93.05	548.83	1.23	

For details on the approach readers are referred to [48]

to different expected maximum fatigue limits in the absence of defects. The fatigue strength of specimens showing a high relative density is on a significantly higher level as compared to specimens with a high number of defects. However, independent of the number of defects, the fatigue strengths assessed in the present work are higher than reported in open literature before. The main conclusion can be drawn as follows:

- (a) By using PBF-LB/M, an intense vaporization of elements can occur, shadowing the laser beam and resulting in lack of fusion defects. Preliminary investigations carried out reveal that the vaporization can be reduced by an optimization of the scan path relative to the gas flow as well as by reducing the layer thickness and the energy input resulting in a higher density of the built parts.

**Fig. 8** Normalized S–N Data of H13 in PBF-EB/M and PBF-LB/M condition. Normalized data for an as-built condition (tested in building direction) of PBF-LB/M processed H13 reported by Pellizzari et al. [28] were recompiled and are included for direct comparison



- (b) The microstructure, which prevails in the PBF-EB/M processed H13 condition, is mainly bainitic including some oval shaped grains of blocky martensite and perlite. In contrast, the higher cooling rates being characteristic for the PBF-LB/M process lead to a predominantly martensitic microstructure. In both cases, phase maps only reveal a minor fraction of face centered cubic structures, eventually indicating only small amounts of retained austenite in the specimens. A preferred crystallographic direction cannot be seen in both conditions.
- (c) The PBF-EB/M state is characterized by a significantly lower mean hardness level ( $471 \pm 36$  HV) compared to the PBF-LB/M state ( $697 \pm 21$  HV). The PBF-EB/M state is characterized by a constant change of hardness values over build height, whereas the hardness in the PBF-LB/M state is more homogeneous. This can be rationalized by the different temperature histories of the different layers in PBF-EB/M and PBF-LB/M.
- (d) The fatigue strength of the PBF-EB/M specimens is higher (500 MPa) than the fatigue strength of the PBF-LB/M counterparts (450 MPa). In addition, a more pronounced scatter in the number of cycles to failure of the PBF-LB/M specimens was observed. Fracture surface analysis as well as the application of the Murakami  $\sqrt{\text{area}}$  concept revealed that the scatter is mainly caused by a higher porosity prevailing in the PBF-LB/M specimens. Moreover, the fatigue limit without defects is mainly influenced by the microstructure. Thus, some PBF-LB/M specimens were able to show superior fatigue strength as compared to PBF-

EB/M material, which is due to the absence of critical defects.

In summary, the results of the present study generally reveal a good fatigue behavior for the additively manufactured tool steel H13 as long as the specimens are characterized by high relative densities. This opens up a wide field of applications in industries where high stresses and number of cycles are paramount. With regard to potential industrial applications, e.g., high pressure die casting and forging, the influence of thermal fatigue as well as thermal shock loading is of highest importance and will therefore be the subject of future studies.

**Acknowledgements** The authors would like to thank voestalpine AG for supply of the powder material from m4p material solutions GmbH and Patrick Wickert M.Sc., Dipl. Ing. Rainer Hunke, Marcel Krochmal M.Sc. and the AM-Team for supporting the experimental work.

**Author contributions** MK, TW, MV, and TN contributed to conceptualization and writing—review and editing; MK and TW helped in methodology; MK done validation, investigation, data curation, writing—original draft preparation, and visualization; TN helped in resources, project administration, and funding acquisition.; MV, TW, and TN helped in supervision. All authors have read and agreed to the published version of the manuscript.

**Funding** Open Access funding enabled and organized by Projekt DEAL.

## Declarations

**Conflict of interest** The authors declare no conflict of interest.

**Open Access** This article is licensed under a Creative Commons Attribution 4.0 International License, which permits use, sharing,



adaptation, distribution and reproduction in any medium or format, as long as you give appropriate credit to the original author(s) and the source, provide a link to the Creative Commons licence, and indicate if changes were made. The images or other third party material in this article are included in the article's Creative Commons licence, unless indicated otherwise in a credit line to the material. If material is not included in the article's Creative Commons licence and your intended use is not permitted by statutory regulation or exceeds the permitted use, you will need to obtain permission directly from the copyright holder. To view a copy of this licence, visit <http://creativecommons.org/licenses/by/4.0/>.

## References

- Körner C (2016) Additive manufacturing of metallic components by selective electron beam melting—a review. *Int Mater Rev* 61:361–377. <https://doi.org/10.1080/09506608.2016.1176289>
- Kranz J, Herzog D, Emmelmann C (2015) Design guidelines for laser additive manufacturing of lightweight structures in TiAl6V4. *J Laser Appl* 27:S14001. <https://doi.org/10.2351/1.4885235>
- Feng S, Kamat AM, Pei Y (2021) Design and fabrication of conformal cooling channels in molds: review and progress updates. *Int J Heat Mass Transf* 171:121082. <https://doi.org/10.1016/j.ijhemastransfer.2021.121082>
- Dimla DE, Camilotto M, Miani F (2005) Design and optimisation of conformal cooling channels in injection moulding tools. *J Mater Process Technol* 164–165:1294–1300. <https://doi.org/10.1016/j.jmatprotec.2005.02.162>
- Seifi M, Salem A, Beuth J et al (2016) Overview of materials qualification needs for metal additive manufacturing. *JOM* 68:747–764. <https://doi.org/10.1007/s11837-015-1810-0>
- Singh R, Gupta A, Tripathi O et al (2020) Powder bed fusion process in additive manufacturing: an overview. *Mater Today Proc* 26:3058–3070. <https://doi.org/10.1016/j.matpr.2020.02.635>
- Kempen K, Yasa E, Thijs L et al (2011) Microstructure and mechanical properties of Selective Laser Melted 18Ni-300 steel. *Phys Procedia* 12:255–263. <https://doi.org/10.1016/j.phpro.2011.03.033>
- Sames WJ, List FA, Pannala S et al (2016) The metallurgy and processing science of metal additive manufacturing. *Int Mater Rev* 61:315–360. <https://doi.org/10.1080/09506608.2015.1116649>
- Wu L, Das S, Gridin W et al (2021) Hot work tool steel processed by laser powder bed fusion: a review on most relevant influencing factors. *Adv Eng Mater* 63:2100049. <https://doi.org/10.1002/adem.202100049>
- Mazur M, Brincat P, Leary M et al (2017) Numerical and experimental evaluation of a conformally cooled H13 steel injection mould manufactured with selective laser melting. *Int J Adv Manuf Technol* 93:881–900. <https://doi.org/10.1007/s00170-017-0426-7>
- Klocke F, Arntz K, Teli M et al (2017) State-of-the-art laser additive manufacturing for hot-work tool steels. *Procedia CIRP* 63:58–63. <https://doi.org/10.1016/j.procir.2017.03.073>
- Outeiro JC (2020) Residual stresses in machining. In: *Mechanics of materials in modern manufacturing methods and processing techniques*. Elsevier, Amsterdam, pp 297–360
- Roberts GA, Krauss G, Kennedy R (1998) *Tool steels*. (5th edn). ASM International, The Materials Information Society, Materials Park
- Guenther E, Kahlert M, Vollmer M et al (2021) Tribological performance of additively manufactured AISI H13 steel in different surface conditions. *Materials* 14:928. <https://doi.org/10.3390/ma14040928>
- Bajaj P, Hariharan A, Kini A et al (2020) Steels in additive manufacturing: a review of their microstructure and properties. *Mater Sci Eng A* 772:138633. <https://doi.org/10.1016/j.msea.2019.138633>
- Krell J, Roettger A, Geenen K et al (2018) General investigations on processing tool steel X40CrMoV5-1 with selective laser melting. *J Mater Process Technol* 255:679–688. <https://doi.org/10.1016/j.jmatprotec.2018.01.012>
- Mertens R, Vrancken B, Holmstock N et al (2016) Influence of powder bed preheating on microstructure and mechanical properties of H13 tool steel SLM parts. *Phys Procedia* 83:882–890. <https://doi.org/10.1016/j.phpro.2016.08.092>
- Rafi HK, Karthik NV, Gong H et al (2013) Microstructures and mechanical properties of Ti6Al4V parts fabricated by selective laser melting and electron beam melting. *J Mater Eng Perform* 22:3872–3883. <https://doi.org/10.1007/s11665-013-0658-0>
- Cormier D, Harrysson A, West H (2004) Characterization of H13 steel produced via electron beam melting. *Rapid Prototyp J* 10:35–41. <https://doi.org/10.1108/13552540410512516>
- Rännar L-E, Glad A, Gustafson C-G (2007) Efficient cooling with tool inserts manufactured by electron beam melting. *Rapid Prototyp J* 13:128–135. <https://doi.org/10.1108/13552540710750870>
- Kahlert M, Brenne F, Vollmer M et al (2021) Influence of microstructure and defects on mechanical properties of AISI H13 manufactured by electron beam powder bed fusion. *J Mater Eng Perform* 30:6895–6904. <https://doi.org/10.1007/s11665-021-06059-7>
- Kirchner A, Klöden B, Franke-Jurisch M et al (2021) Manufacturing of tool steels by PBF-EB. *Metals* 11:1640. <https://doi.org/10.3390/met11101640>
- Cardeal G, Sequeira D, Mendonça J et al (2021) Additive manufacturing in the process industry: a process-based cost model to study life cycle cost and the viability of additive manufacturing spare parts. *Procedia CIRP* 98:211–216. <https://doi.org/10.1016/j.procir.2021.01.032>
- Chadha U, Abrol A, Vora NP et al (2022) Performance evaluation of 3D printing technologies: a review, recent advances, current challenges, and future directions. *Prog Addit Manuf* 7:853–886. <https://doi.org/10.1007/s40964-021-00257-4>
- Wood WA (1958) Formation of fatigue cracks. *Phil Mag* 3:692–699. <https://doi.org/10.1080/14786435808237004>
- Sanaei N, Fatemi A (2021) Defects in additive manufactured metals and their effect on fatigue performance: a state-of-the-art review. *Prog Mater Sci* 117:100724. <https://doi.org/10.1016/j.pmatsci.2020.100724>
- Dörfert R, Zhang J, Clausen B et al (2019) Comparison of the fatigue strength between additively and conventionally fabricated tool steel 1.2344. *Addit Manuf* 27:217–223. <https://doi.org/10.1016/j.addma.2019.01.010>
- Pellizzari M, AlMangour B, Benedetti M et al (2020) Effects of building direction and defect sensitivity on the fatigue behavior of additively manufactured H13 tool steel. *Theoret Appl Fract Mech* 108:102634. <https://doi.org/10.1016/j.tafmec.2020.102634>
- (1997) *ASM handbook, Volume 1: properties and selection: irons, steels, and high-performance alloys*, 5. print. ASM International, Metals Park
- Garcias JF, Martins RF, Branco R et al (2021) Quasistatic and fatigue behavior of an AISI H13 steel obtained by additive manufacturing and conventional method. *Fatigue Fract Eng Mater Struct* 44:3384–3398. <https://doi.org/10.1111/ffe.13565>
- Macek W, Martins RF, Branco R et al (2022) Fatigue fracture morphology of AISI H13 steel obtained by additive manufacturing. *Int J Fract* 235:79–98. <https://doi.org/10.1007/s10704-022-00615-5>
- Chadha U, Selvaraj SK, Abraham AS et al (2023) powder bed fusion via machine learning-enabled approaches. *Complexity* 2023:1–25. <https://doi.org/10.1155/2023/9481790>

33. Ackermann M, Haase C (2023) Machine learning-based identification of interpretable process-structure linkages in metal additive manufacturing. *Addit Manuf* 71:103585. <https://doi.org/10.1016/j.addma.2023.103585>
34. Grierson D, Rennie AEW, Quayle SD (2021) Machine learning for additive manufacturing. *Encyclopedia* 1:576–588. <https://doi.org/10.3390/encyclopedia1030048>
35. Niendorf T, Klimala P, Maier HJ et al (2012) The role of notches on fatigue life of TWIP steel in the HCF regime. *MSF* 706–709:2205–2210. <https://doi.org/10.4028/www.scientific.net/MSF.706-709.2205>
36. Richter J, Sajadifar SV, Niendorf T (2021) On the influence of process interruptions during additive manufacturing on the fatigue resistance of AlSi12. *Addit Manuf* 47:102346. <https://doi.org/10.1016/j.addma.2021.102346>
37. Angeli J, Füreder E, Panholzer M et al (2006) Ätztechniken für die Phasencharakterisierung von niedriglegierten Dual-Phasen- und TRIP-Stählen. *Pract Metallogr* 43:489–504. <https://doi.org/10.3139/147.100315>
38. Bargel H-J, Schulze G (2012) *Werkstoffkunde*. Springer, Berlin
39. Hearn W, Lindgren K, Persson J et al (2022) In situ tempering of martensite during laser powder bed fusion of Fe-0.45C steel. *Materialia* 23:101459. <https://doi.org/10.1016/j.mtla.2022.101459>
40. Keul C, Wirths V, Bleck W (2012) New bainitic steels for forgings. *Arch Civ Mech Eng* 12:119–125. <https://doi.org/10.1016/j.acme.2012.04.012>
41. Kind & Co Edelstahlwerk Datasheet Dominial USD 1.2344. [http://www.kindtakimcelik.com/de/\\_download/warmarbeitskatalog.pdf](http://www.kindtakimcelik.com/de/_download/warmarbeitskatalog.pdf). Accessed 31 May 2021
42. Cahn RW, Haasen P (1996) *Physical metallurgy*, 4th edn. Elsevier Science, Amsterdam
43. Pešička J, Kužel R, Dronhofer A et al (2003) The evolution of dislocation density during heat treatment and creep of tempered martensite ferritic steels. *Acta Mater* 51:4847–4862. [https://doi.org/10.1016/S1359-6454\(03\)00324-0](https://doi.org/10.1016/S1359-6454(03)00324-0)
44. Pang JC, Li SX, Wang ZG et al (2014) Relations between fatigue strength and other mechanical properties of metallic materials. *Fatigue Fract Eng Mater Struct* 37:958–976. <https://doi.org/10.1111/ffe.12158>
45. Zerbst U, Bruno G, Buffiere J-Y et al (2021) Damage tolerant design of additively manufactured metallic components subjected to cyclic loading: state of the art and challenges. *Progress Mater Sci* 121:100786. <https://doi.org/10.1016/j.pmatsci.2021.100786>
46. Murakami Y, Endo M (1986) Effects of hardness and crack geometry on DELTA.Kth of small cracks. *J Soc Mater Sci, Japan* 35:911–917. <https://doi.org/10.2472/JSMS.35.911>
47. Murakami Y (2005, cop. 2002) *Metal fatigue: effects of small defects and nonmetallic inclusions*, Reprint. Elsevier, Amsterdam
48. Murakami Y, Takagi T, Wada K et al (2021) Essential structure of S-N curve: Prediction of fatigue life and fatigue limit of defective materials and nature of scatter. *Int J Fatigue* 146:106138. <https://doi.org/10.1016/j.ijfatigue.2020.106138>
49. Murakami Y, Endo M (1994) Effects of defects, inclusions and inhomogeneities on fatigue strength. *Int J Fatigue* 16:163–182. [https://doi.org/10.1016/0142-1123\(94\)90001-9](https://doi.org/10.1016/0142-1123(94)90001-9)
50. Sochalski-Kolbus LM, Payzant EA, Cornwell PA et al (2015) Comparison of residual stresses in inconel 718 simple parts made by electron beam melting and direct laser metal sintering. *Metall Mater Trans A* 46:1419–1432. <https://doi.org/10.1007/s11661-014-2722-2>

**Publisher's Note** Springer Nature remains neutral with regard to jurisdictional claims in published maps and institutional affiliations.